Triple-picket warm plastic-shell implosions on OMEGA

P. B. Radha,[1] C. Stoeckl,[1] V. N. Goncharov,[1] J. A. Delettrez,[1] D. H. Edgell,[1] J. A. Frenje,[2]
I. V. Igumenshchev,[1] J. P. Knauer,[1] J. A. Marozas,[1] R. L. McCrory,[1,3]
D. D. Meyerhofer,[1,3] R. D. Petrasso,[3] S. P. Regan,[1] T. C. Sangster,[1] W. Seka,[1]
and S. Skupsky[1]

[1]*Laboratory for Laser Energetics, University of Rochester, 250 East River Road, Rochester,
New York 14623-1299, USA*
[2]*Plasma Fusion Science Center, Massachusetts Institute of Technology, 77 Massachusetts Avenue,
Cambridge, Massachusetts 02139, USA*
[3]*Department of Mechanical Engineering and Department of Physics, University of Rochester,
250 East River Road, Rochester, New York 14623-1299, USA*

Warm deuterium-gas-filled plastic shells are imploded by direct irradiation from the OMEGA laser
[T. R. Boehly *et al.*, Opt. Commun. **133**, 495 (1997)]. The pulse shapes contain three pickets that
precede a sharp rise to a constant laser intensity at $\sim 4.5 \times 10^{14}$ W/cm^2. The in-flight-aspect-ratio
(IFAR), a crucial measure of shell instability to nonuniformity growth, is varied in these implosions
by changing picket energies and the timing among the pickets. Simulations that include cross-beam
energy transfer in addition to inverse bremsstrahlung for the laser-energy deposition models show
better agreement with measurements of the neutron bang time and temporally resolved scattered
light and therefore more correctly model the shell kinetic energy. It is also shown that target
performance improves significantly as IFAR is reduced. Nearly twice the neutron yield is measured
for IFAR ~ 31 compared to IFAR ~ 60. The ratio of the measured to simulated neutron yield and
areal density increases significantly with decreasing IFAR. These implosions unambiguously link
target performance to in-flight shell instability attributable to short-wavelength growth and indicate
that IFAR ≤ 40 is required to achieve adequate compression at this intensity. © *2011 American
Institute of Physics*. [doi:10.1063/1.3544930]

I. INTRODUCTION

In direct-drive inertial confinement fusion nominally
identical beams of a laser irradiate a gas-filled spherical
capsule.[1] The capsule material ablates, accelerating the rest
of the shell inward. In an igniting capsule, made from cryo-
genic deuterium-tritium (DT), the hot spot, formed by the
PdV work of the colder, higher-density converging shell, has
a temperature of ~ 10 keV with an areal density of
~ 300 mg/cm^2. Under these conditions, the ~ 3.5 MeV al-
pha particles produced from the DT reactions redeposit their
energy in the compressed core, increasing the temperature
and the volume over which fusion reactions can occur. Con-
sequently, the energy produced from fusion reactions can be
greater than the incident laser energy.

A key measure of target performance is the profile of the
adiabat in the shell, where the adiabat is defined as the ratio
of the pressure to the Fermi-degenerate pressure. The adiabat
profile is selected through an optimal choice of the laser
temporal history used to irradiate the implosion. For reasons
explained in what follows, the adiabat profile is chosen such
that it has a low value on the inside of the shell and a high
value on the outside of the shell at the surface where the
ablation takes place. Several measures of this adiabat profile
are important to characterize the implosion. The adiabat on
the inside of the shell, α_{inn}, defined as the ratio of the Fermi-
degenerate pressure at peak shell density determines the
minimum energy required for ignition, E_{min}. This quantity
has been shown to depend on α_{inn}, the velocity of the shell at

maximum kinetic energy, the implosion velocity V_{imp}, and
the pressure on the outside of the fuel when it reaches the
implosion velocity, P (Ref. 2), and is given by

$$E_{\mathrm{min}}(\mathrm{kJ}) = 50.8 \alpha_{\mathrm{inn}}^{1.88} \left(\frac{V_{\mathrm{imp}}}{3 \times 10^7 \ \mathrm{cm/s}} \right)^{-5.89}$$
$$\times \left(\frac{P}{100 \ \mathrm{Mbar}} \right)^{-0.77}. \tag{1}$$

For a laser wavelength of 0.351 μm, this can be rewritten in
terms of the in-flight-aspect-ratio (IFAR), defined as the ratio
of the average shell radius (R) to the in-flight shell thickness
(Δ_{if}). IFAR can be written in terms of $\langle \alpha \rangle$, the density-
averaged adiabat in the shell—another measure of the adia-
bat profile,

$$\mathrm{IFAR} = \frac{R}{\Delta_{\mathrm{if}}} = \frac{60(V_{\mathrm{imp}}/3 \times 10^7 \ \mathrm{cm/s})^2}{\langle \alpha \rangle^{0.6} I_{15}^{0.27}}, \tag{2}$$

where the pressure $P(\mathrm{Mbar}) = 80 I_{15}^{2/3}$ and I_{15} is the on-target
laser intensity in units of 10^{15} W/cm^2 (Ref. 1). The mini-
mum energy required for ignition can be equivalently written
in terms of IFAR as

$$E_{\mathrm{min}}(\mathrm{kJ}) = 1.3 \times 10^7 \left(\frac{\alpha_{\mathrm{inn}}}{\langle \alpha \rangle} \right)^{1.8} \frac{1}{(\mathrm{IFAR})^3 I_{15}^{1.3}}. \tag{3}$$

For a given adiabat profile in the shell, a high IFAR is re-
quired to reduce the minimum energy at which ignition can
occur.

A high IFAR can compromise target performance through the growth of nonuniformities. Nonuniformities are seeded by laser-beam variations, laser speckle from individual laser beams, and target nonuniformities. As the shell accelerates inward, the Rayleigh–Taylor (RT)[1,3] instability causes these nonuniformities at the outer ablation surface to grow. Depending on their wavelength, these distortions can compromise the compression and can additionally decrease neutron yields by reducing the temperature and volume of the hot spot.[4] The RT growth rate can be written as $\gamma = 0.94\sqrt{kg} - 2.7kV_a$ (Ref. [5]), where k is the wave number, g is the acceleration, and $V_a \sim \alpha_{out}^{0.6} I_L^{0.07}$ is the ablation velocity, where α_{out} is the adiabat at the ablation surface and I_L is the laser intensity. The most dangerous modes that cause the in-flight shell to break up are given by $k\Delta_{if} \approx 1$. Substituting the expression for IFAR in Eq. (23) of Ref. [6], the number of e-foldings experienced by the most dangerous mode can be written as

$$N_e(k\Delta_{if} = 1) = \gamma(k\Delta_{if} = 1)t$$

$$\approx \sqrt{\text{IFAR}}\left[1 - \frac{0.09\alpha_{out}^{0.3}}{I_{15}^{0.2}}\left(\frac{\alpha_{out}}{\langle\alpha\rangle}\right)^{0.3}\right]. \quad (4)$$

This suggests that a low IFAR with a higher adiabat at the ablation surface is more optimal for reducing instability growth. Verifying the optimal range of IFAR experimentally is crucial in making the optimal choice for an ignition design. As shown so far, the trade-off in IFAR can be derived from well-known scaling laws. To our knowledge, this is the first experimental study of the performance of capsule implosions which use pulse shape variations to achieve a calculated variation in IFAR between 30 and 60. Moreover, the laser pulse shape used in this work is very similar to the one used for the direct-drive-ignition design[7] for the National Ignition Facility.

Several implosion observables are used to study target performance and to test both spherically symmetric [one-dimensional (1D)] and nonuniformity [two-dimensional (2D)] modeling. Since IFAR $\sim V_{imp}^2$ [Eq. (3)] it is crucial to verify that the design implosion velocity has been achieved in implosion experiments. The implosion velocity depends on the laser energy absorbed and the extent of heat conduction to the ablation surface, the physics of which is primarily 1D and only marginally influenced by nonuniformity. Scattered light is measured during the implosion to infer the extent of laser-energy absorption in the corona. For typical temperatures in these implosions, the neutron yield Y_{1n} scales with the density ρ, and ion temperatures T_i in the fuel, as $Y_{1n} \sim \int \rho^2 T_i^4 d^3 r dt$. Since $T_i \sim \langle\alpha\rangle^{-0.15} V_{imp}^{1.3}$ (Ref. [8]), the total 1D neutron yield is determined by implosion velocity. Y_{1n} can be compromised by nonuniformity growth through the reduction of core density and temperatures in addition to the volume and the duration over which neutrons are produced. The time of neutron production ("bang time") is another important observable related to the shell kinetic energy and therefore the implosion velocity. As discussed in Sec II, bang time is also determined, however, by the extent of nonuniformity growth during acceleration. The measured scattered light and neutron rates are compared with simulations, and it will be shown that better agreement between simulation and measurement is obtained when cross-beam laser-energy transfer induced by stimulated Brillouin scattering (SBS) (Ref. [9]) is included in addition to inverse bremsstrahlung for the laser-deposition models in simulation.

The observed areal density can be reduced relative to simulations for several reasons. It has been shown that the maximum areal density ρR_{max} attainable in an implosion depends primarily on the laser energy E_L and α_{inn} (Ref. [10]),

$$\rho R_{max}(\text{mg/cm}^2) = \frac{2.6 \times 10^2 E_L^{1/3}(\text{kJ})}{\alpha_{inn}^{0.6}}. \quad (5)$$

Implosions in this work are irradiated with a triple-picket laser pulse. Shocks caused by each of the three pickets in the laser pulse and the main shock caused by the laser pulse must catch up just as they break out from the shell. A higher adiabat at the inside of the shell can be obtained, for example, by mistiming shocks, i.e., launching shocks such that they meet too early on the inside of the shell or too late after they have all broken out of the shell.

Different measures of the adiabat profile in the shell (α_{inn}, α_{out}, and $\langle\alpha\rangle$) enter into the various hydrodynamic relationships described above. The IFAR trade-off indicates that a high α_{out} and a low α_{inn} will provide optimal performance. Pickets have been previously used to achieve such a shaping of the adiabat profile in the shell.[11] These pulse shapes consisted of a single picket followed by a continuous rise to constant peak intensity. The picket sets the adiabat and the continuous rise is used to launch a compression wave to allow for the target to compress adiabatically. It was, however, observed that compression was significantly compromised with these continuous pulses in cryogenic implosion experiments. Separate experiments that measured the timing of the shock and the compression wave suggested deviations in the compression wave from modeled behavior and indicated that the compression wave steepened into a shock, thereby raising the adiabat.[12] Multiple-picket pulse shapes have been used to avoid launching a compression wave. Each picket launches a shock, and proper timing requires that these shocks catch up just at shock breakout from the shell. High compression has been achieved with these pulse shapes in cryogenic implosions with neutron-averaged areal density $\langle\rho R\rangle \sim 300$ mg/cm^2 (Ref. [7]). Shock-timing experiments have also indicated that the shocks are adequately modeled for a range of picket energies in both cryogenic and warm plastic shells.[12]

In addition to shock mistiming, the areal density can be potentially compromised by preheat from energetic electrons or radiation from the corona. Since the intensity used in these implosions is very close to the threshold of the two-plasmon-decay (TPD) instability,[13] preheat from energetic electrons is not an issue in this work. As shown in Ref. [14], coronal radiation plays an important role in these implosions, but since it is included in all the modeling, it is not discussed further.

Nonuniformity growth can influence the areal density in implosion experiments in two ways: as will be shown in this paper, long-wavelength perturbations ($\ell \leq 20$) decrease the

clean volume and the duration over which neutrons are produced (also referred to as "burn truncation") while achieving near-1D compression. Since areal density is inferred experimentally through fusion products, the different neutron-production histories can apparently reduce the inferred areal density relative to 1D simulation. Shorter-wavelength non-uniformities, on the other hand, can cool the hot core, thereby reducing the neutron yield, and can also reduce compression by raising the adiabat in the converging shell. This reduces the actual areal density achieved relative to 1D while also introducing an apparent areal-density reduction because of a different neutron-production history.

Understanding and modeling the various sources of non-uniformity are important for validating ignition modeling and designs. Warm plastic shells have the advantage that they can be imploded frequently and are highly repeatable, allowing controlled studies. This paper describes directly driven warm plastic shell implosions using triple-picket laser pulse shapes. Picket energies and the timing between the pickets are varied to change the modeled IFAR of the target. It is shown that the observed areal density is significantly reduced from the spherically symmetric (1D) modeled values, using the hydrodynamic code *LILAC*,[15] when IFAR ∼60. When short-wavelength nonuniformities are accounted for in 2D simulations using the code *DRACO*,[14] the areal density is also reduced, consistent with the observations. When IFAR is reduced by increasing picket energies, simulations predict areal densities closer to the spherically symmetric model when multidimensional effects are included. This is also consistent with observation. Neutron yields show consistent trends: when IFAR is reduced, observed neutron yields increase, while the 1D simulated values decrease, indicating better shell stability.

This paper is organized as follows. Section II discusses the physics of triple-picket implosions, including the effect of the various sources of nonuniformity. Section III presents the experimental observations. The conclusions are presented in Sec. IV.

II. TRIPLE-PICKET IMPLOSIONS

The OMEGA (Ref. 16) laser is used to irradiate 9 atm deuterium (D_2)-filled, 27-μm-thick plastic (CH) shells with 860 μm nominal diameter (Fig. 1). The temporally varying laser pulse shape is also shown in Fig. 1. Approximately 18 kJ of energy is incident on the target with peak intensity of ∼4.5×10^{14} W/cm^2 ($I_{15} \sim 0.45$). Different smoothing levels[17] [1 color cycle (cc): 1 THz smoothing by spectral dispersion (SSD); 3 cc: 1/3 THz SSD; and laser irradiation with no bandwidth] were employed to empirically study the effect of laser nonuniformity on-target performance. Phase plates with super-Gaussian order of ∼4 (Ref. 18) and polarization smoothing[19] were used. The laser energy on target was set by the constraints of the OMEGA Laser System, whereas the laser intensity was chosen to extend the length of the laser drive so that the pressure on the outside of the imploding fuel was maintained until the shell began to decelerate, which made it possible for the implosion to achieve the maximum compression possible for this laser energy.
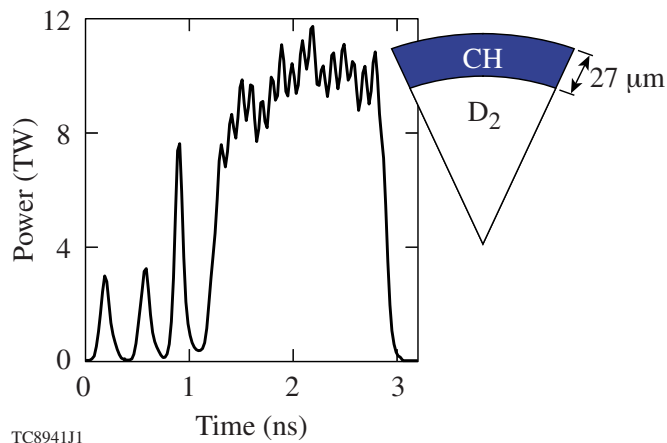
FIG. 1. (Color online) Typical laser pulse shape and target.

TC8941J1

For the shell diameter, thickness, energy, and intensity chosen, the calculated implosion velocity $V_{imp}=2.6 \times 10^7$ cm/s. Since the IFAR scales as the square of the implosion velocity [Eq. (2)], changing the implosion velocity gives the highest leverage on IFAR. Increasing the implosion velocity requires smaller or thinner, less-massive targets or an increase in the on-target laser energy. Thinner or smaller shells require challenging pulse shapes because of the short time separation between the pickets and between the third picket and the main pulse; most of the implosions considered here use the nominal target size described in the previous paragraph. Moreover, keeping the same target dimensions allows a systematic study by varying only laser parameters. However, to achieve the highest IFAR studied in this work, IFAR ∼60, a combination of pulse shapes and smaller targets (∼830 μm diameters) has been used. As a result of the less-massive shells, the IFAR ∼60 implosions have $V_{imp}=2.8 \times 10^7$ cm/s.

As Eq. (2) indicates, the IFAR can also be changed by changing the adiabat profile and therefore $\langle \alpha \rangle$ in the shell. On the OMEGA laser, controlled IFAR variation can be more easily achieved by changing the temporal variation of the incident on-target laser intensity and therefore through a variation in $\langle \alpha \rangle$. The adiabat profile is primarily set by timing shocks from the three pickets and the main pulse, such that they meet near shock breakout. Lower picket energies result in weaker shocks and a lower adiabat at the back of the shell. The shocks for each IFAR are optimally timed in 1D simulations by changing picket energies and timings using the hydrodynamic code LILAC. As mentioned earlier, shock timing experiments indicate that shock velocities and catch-up times are modeled accurately for these pulse shapes, providing independent confirmation of the simulated shell adiabat. This provides confidence in the simulated changes in IFAR with changes in the input laser irradiation.

As the shell converges, it becomes thicker and, as a result, the IFAR decreases as the implosion proceeds. In Eq. (2) the IFAR is defined in terms of an average radius, which is somewhat subjective. In this work, the IFAR is defined at a time when the shell has traveled ∼100 μm—1/3 of the total distance traveled during acceleration. The modeled
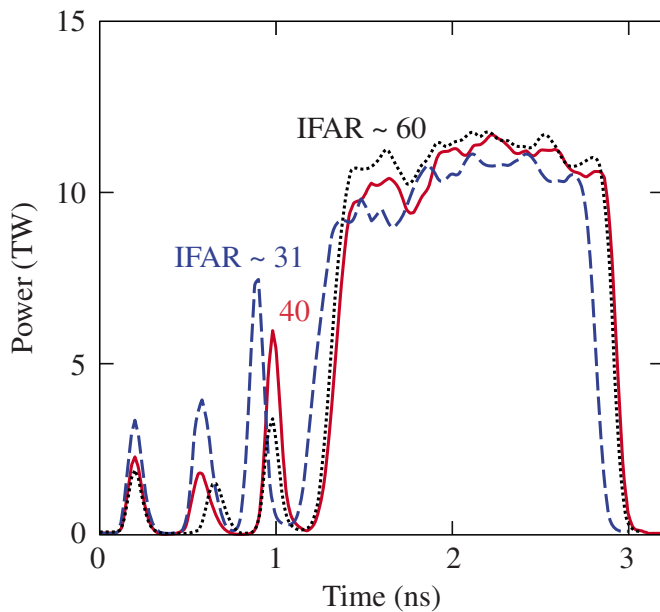
FIG. 2. (Color online) Variations in the laser pulse shapes to achieve a different IFAR.

FIG. 3. (Color online) Amplitudes at the start of the acceleration phase for an IFAR ~ 60 implosion (open) and an IFAR ~ 31 implosion (closed).

IFAR varies in value from ~ 31 to ~ 60 with $(\alpha_{out}/\langle\alpha\rangle) \sim 5$ and $(\alpha_{inn}/\langle\alpha\rangle) \sim 0.6$ for each IFAR. These different pulse shapes used on the OMEGA laser are shown in Fig. 2. The factor by which the shell converges during the implosion is the convergence ratio CR $[CR = R_i/R_f$, where R_i is the initial inner radius of the shell and R_f is the radius of the shell at stagnation (defined at the $1/e$ location of peak density) that varies between 23 and 25, comparable to the convergence in current OMEGA cryogenic implosions (21–23)].

   To understand the effects of the various sources of non-uniformity, two-dimensional simulations using the hydrodynamic code DRACO were performed using nominal target dimensions and laser pulse shapes for each value of IFAR. Inverse-bremsstrahlung laser-energy deposition with flux-limited heat conduction (with a sharp-cutoff flux limiter of 0.06) and 48-group diffusive radiation transport is used to model the 2D implosions in this paper (also later referred to as the "standard model"). It has been shown that cross-beam transfer of energy induced by SBS can reduce the available laser energy to provide the shell with its kinetic energy.[9] Ion-acoustic waves transfer energy from incoming laser rays to outgoing laser rays, significantly decreasing the laser energy deposited near their turning points. Cross-beam effects are significant during the main part of the laser pulse when a plasma atmosphere is well established and the matching conditions for ion-acoustic waves are met over a large spatial range in the corona. This is accounted for in 2D simulations by reducing the power by 15% during the main part of the pulse. With this reduction, shell trajectories and densities match those in 1D simulations, where a more-detailed model explicitly accounts for cross-beam effects.

   The effect of single-beam speckle is examined using simulations of laser imprint and is modeled as described in Ref. 14. To quantify the magnitude of the nonuniformity seeds, each ℓ mode is simulated individually with 1 cc,
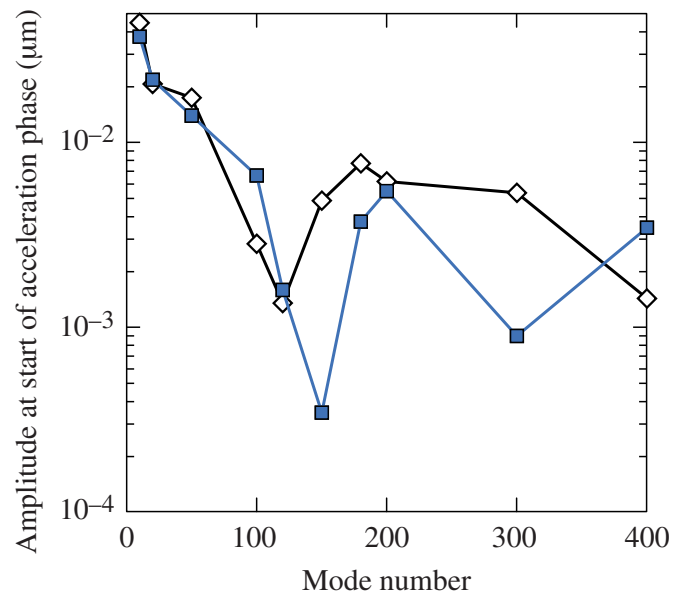
1 THz smoothing for modes up to $\ell = 400$ for implosions with differing IFAR. As Fig. 3 shows, the amplitude seeds for the acceleration phase do not differ significantly between the extreme IFAR implosions; IFAR ~ 31 with the higher picket energies and the IFAR ~ 60 implosions with the lower picket energies have similar imprint amplitudes. These amplitudes are similar to the amplitudes calculated for cryogenic targets.[20]

   Multimode simulations up to $\ell = 400$ are performed on an 18° wedge with 200 angular zones, corresponding to a resolution of ten zones/wavelength for the shortest wavelength simulated. Single mode simulations with realistic imprint amplitudes indicate that modes $\ell < 300$ are the most dangerous for in-flight shell stability for these designs. For $\ell = 300$, this resolution in these simulations is ~ 13 zones/wavelength, where numerical convergence to within 3% is achieved for RT growth rates. For $I_L \sim 4.5 \times 10^{14}$ W/cm^2, good agreement has been obtained previously for single-mode growth rates between simulation and separate experiments in planar geometry[21] using DRACO, lending some confidence to the multimode simulations. Density contours at the end of the acceleration phase (Fig. 4) indicate that the shell is integral for the IFAR ~ 31 implosion and is significantly distorted ("broken" since portions of the shell are at less than solid density) for the IFAR ~ 60 implosion. Since the imprint amplitudes are very similar between the two implosions, this difference in shell stability is due to increased RT growth rates for the higher IFAR implosion. The most dangerous mode has a mode number $\ell \sim 30$ with an in-flight shell thickness $\Delta_{if} \sim 10$ μm at a shell radius of 300 μm and corresponds to a wavelength $\lambda = 2\pi R/\ell \sim 60$ μm. According to Eq. (4), growth rates for the most dangerous modes scale as $\sqrt{\text{IFAR}}$, leading to higher growth rates for IFAR ~ 60 relative to IFAR ~ 31. Modes near $\ell \sim 30$ alone, however, are insufficient to compromise shell integrity. When modes up to $\ell = 60$, which include the most dangerous modes but exclude
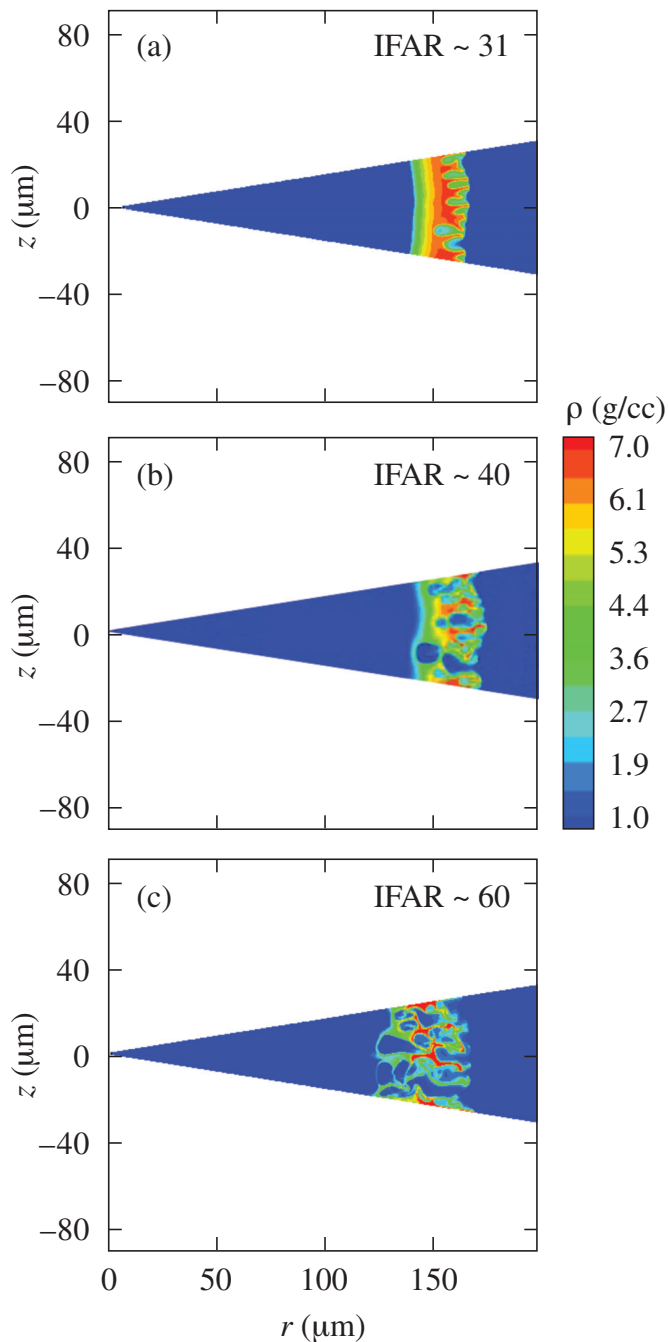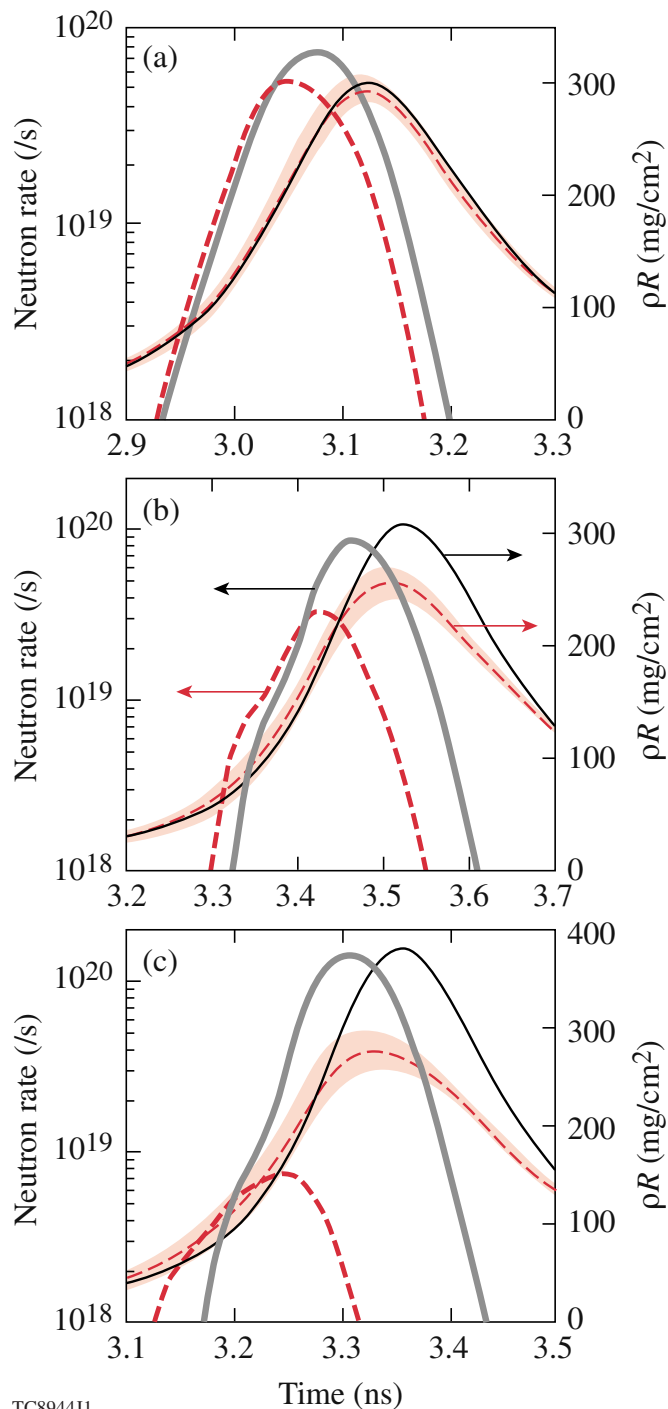
FIG. 4. (Color) Density contours at the end of the acceleration phase for implosions with (a) IFAR ∼ 31, (b) IFAR ∼ 40, and (c) IFAR ∼ 60. Only the effect of laser imprint is simulated using single-beam nonuniformity as the seeds.

TC8944J1

FIG. 5. (Color online) Left axis: neutron-rate history for the spherically symmetric implosion (thick solid line) compared to the implosion with laser imprint as the nonuniformity seed (thick dashed) for (a) IFAR ∼ 31, (b) IFAR ∼ 40, and (c) IFAR ∼ 60 implosions. Right axis: areal-density history from 2D simulations (thin dashed) for the same implosions with the corresponding spherically symmetric results shown as a thin solid line. The shaded regions indicate the variation in areal density in the polar angle around the target.

shorter wavelengths, are included in an IFAR ∼ 60 simulation, the shell remains integral at the end of the acceleration phase and is only marginally distorted. Highly nonlinear growth of the short wavelengths is required to feed the amplitude of the longer, more-dangerous modes. Growth of long wavelengths in the presence of highly nonlinear, short-wavelength-mode growth has been observed previously in the laser-driven planar experiments in Ref. 21.

Shell distortion during the acceleration phase reduces the areal density achieved in the implosion. The areal-density histories for the implosions with varying IFAR are shown in

Fig. 5. When the shell is integral, 2D simulations recover the areal-density history of the spherically symmetric implosions, whereas peak values of areal density are only ∼70% of 1D when the shell is broken. In contrast, when the simulation includes only modes up to $\ell = 60$, nearly 96% of the peak areal density is achieved, indicating that short-

wavelength growth is crucial to compromising compression. Cross-beam-energy-transfer effects have a marginal effect on nonuniformity growth; for the IFAR∼60 implosion, peak areal density is ∼72% of 1D when cross-beam effects are included (using the prescription of lowering the on-target intensity) compared to ∼70% of 1D when they are not included. Figure 5 shows that the neutron rates are increasingly advanced relative to spherically symmetric simulations for increasing IFAR (or increasing shell distortion), despite the similar implosion velocities. A broken shell is at a much lower density and occupies more volume and therefore is thicker than an integral shell. Consequently, the rebounding shock interacts with the shell decelerating it earlier. This causes an earlier neutron production compared to an intact shell. The most-extreme shift of neutron-production history is calculated for the IFAR∼60 implosion; 2D simulations indicate that the neutron-production history is advanced by ∼50 ps.

The effect of longer wavelengths is shown in Fig. 6 for the IFAR∼60 implosion. For each simulation, one random realization is drawn from a Gaussian distribution with nominal values of nonuniformities: 60-beam port locations on OMEGA, mistiming between the beams (10 ps rms), mispointing errors of the beams (10 μm rms), and energy imbalance among the OMEGA beams (2.6% rms). The 60 OMEGA beams are then projected on a sphere and the amplitudes of the spherical harmonics are added in quadrature to obtain the seeds for the axisymmetric DRACO simulation. The phase of the $m=0$ mode is chosen as the phase of the simulated mode. The simulations include modes up to $\ell=20$. Density distortions at peak neutron production (Fig. 6) are dominated by the mode corresponding to OMEGA geometry ($\ell\sim20$). The lineout of areal density versus polar angle from the same time slice is also shown in Fig. 6(b). The average 2D value (dashed line) compares very well to the spherically symmetric value (solid line). These simulations indicate that long-wavelength nonuniformities primarily introduce areal-density variations without significantly compromising the average value.

The effect of nonuniformity on implosion observables is summarized in Fig. 7. The ratio of the neutron yield from 2D simulation to the spherically symmetric simulation decreases significantly with IFAR when only the imprint is included (solid circles) and shows a weak dependence on IFAR for the longer-wavelength perturbations (open circles). Similarly, the fraction of the 1D peak areal density recovered in 2D simulations decreases with increasing IFAR only for short-wavelength nonuniformity growth (solid circles). When only long-wavelength perturbations (open circles) are considered, significant variation in the angular value of areal density is simulated. The "error bars" represent the minimum and maximum values of areal density around the polar angle in the simulation. No degradation in the average value is simulated for only long-wavelength perturbations. As mentioned in Sec. I, the actual neutron-averaged value of areal density $\langle\rho R\rangle$ inferred in experiments will depend on the details of the neutron-production history.

Long-wavelength nonuniformities do not change the neutron-averaged ion temperature (open circles) [Fig. 7(c)],
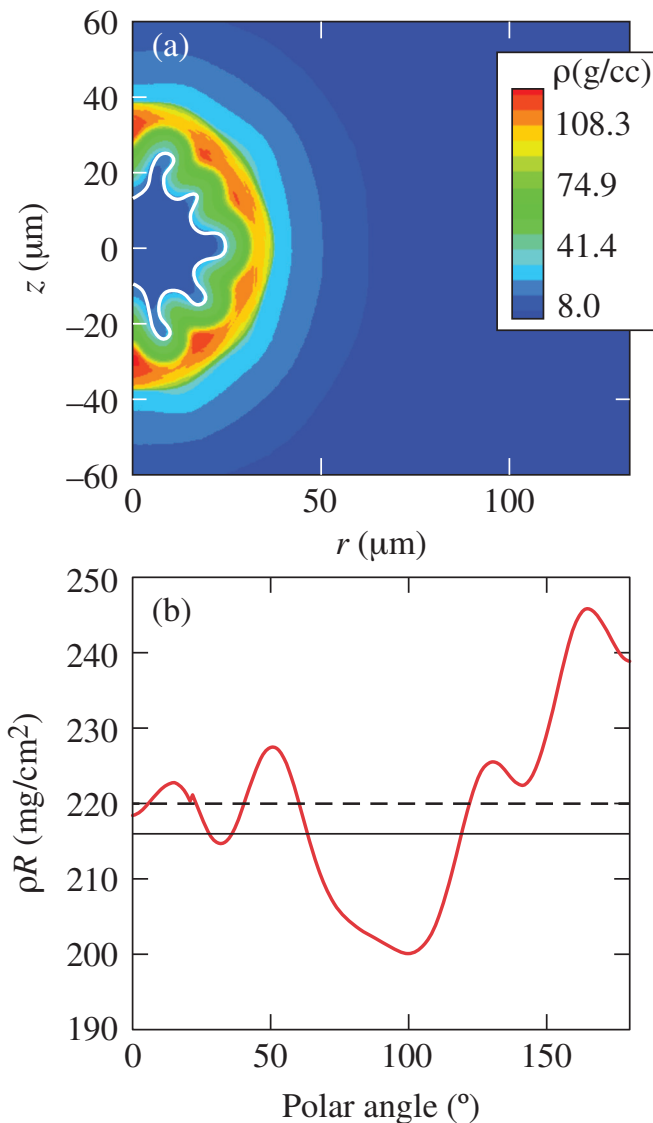

FIG. 6. (Color) (a) Density contours at peak neutron production due to beam-beam imbalances, including beam energy imbalance (5%), beam mispointing (10 μm rms), and beam mistiming (9 ps rms) for the IFAR ∼ 31 implosion. The white contour marks the location of the D_2–CH interface. (b) Simulated polar angle variations of areal density for the 2D simulation in (a) (solid) and spherically symmetric simulation (light solid). The average of the 2D simulation is shown as a dashed line.

defined from the width of the neutron time-of-flight spectrum. The decrease in neutron yield when long-wavelength perturbations are included has been shown previously to be mainly due to the reduction in the volume of the neutron-producing region and mass flow into the colder bubbles near the fuel-shell interface.[22] Shorter-wavelength perturbations significantly decrease the ion temperatures in the core (solid circles). The yield reduction, in this case, is due to the reduced compression and also lower temperatures.

The experimental results are discussed in Sec. III.

III. OBSERVATIONS

Information on implosion energetics can be obtained through a detailed comparison of simulated and measured scattered light and neutron bang times. Figure 8(a) shows the measured scattered light[23] compared to different models in a
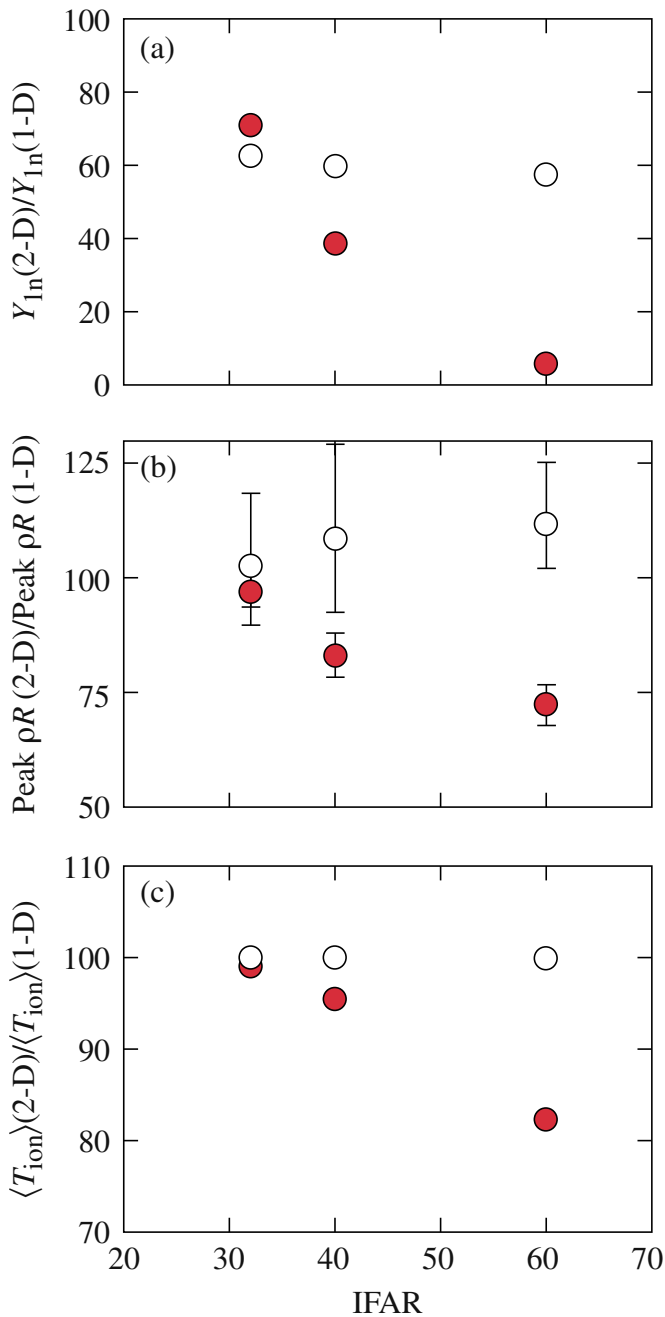
FIG. 7. (Color online) (a) The 2D yield relative to the spherically symmetric yield for various sources of nonuniformity: imprint (solid), beam-beam imbalances (open) vs the calculated IFAR. (b) Average peak areal density from 2D simulations relative to the spherically symmetric areal density for the same sources of nonuniformity vs IFAR. The error bars indicate the variation in areal density vs polar angle in the simulation. (c) Ratio of neutron-averaged ion temperatures from 2D simulations to those from spherically symmetric simulations vs IFAR.
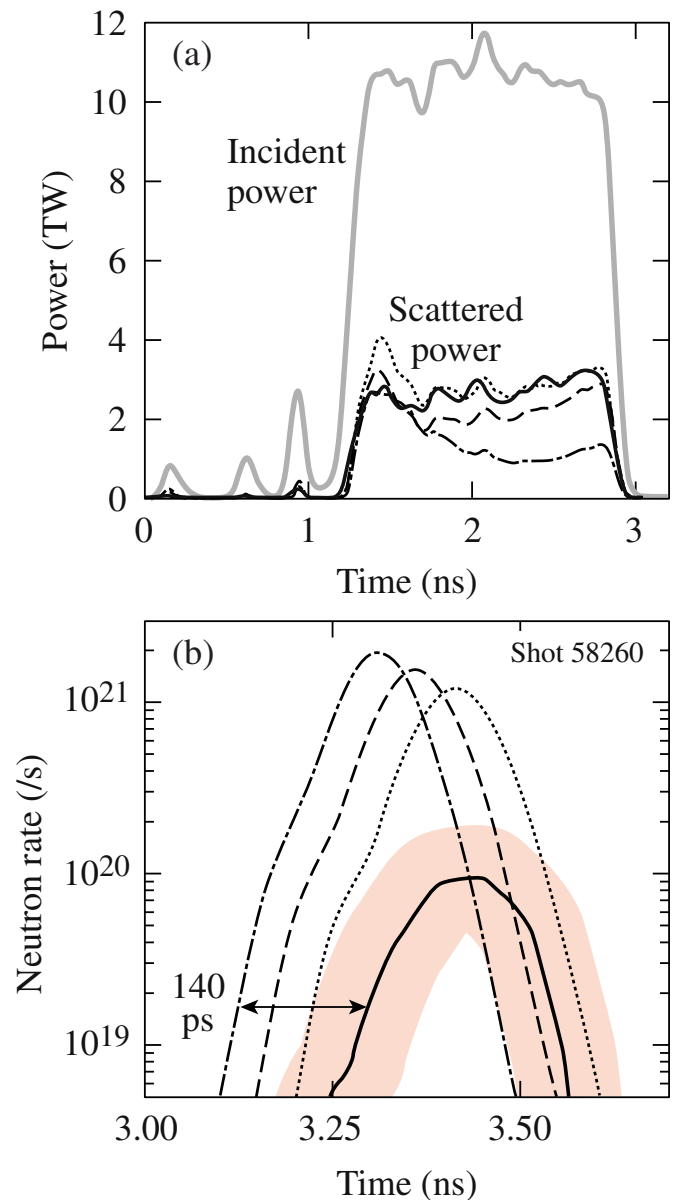

FIG. 8. (Color online) (a) Laser pulse shape (light). Temporally resolved scattered light measured (solid), simulated with the flux-limited model (dashed-dot), simulated with the cross-beam transfer model with a multiplier of 0.5 (dashed), and simulated with the cross-beam transfer model with a multiplier of 1.0 (dotted). (b) Measured neutron-rate history (solid) and simulated neutron-rate history with the flux-limited thermal transport model (dashed-dotted), and laser-deposition model including the effect of cross-beam energy transfer with a multiplier of 0.5 (dashed) and a multiplier of 1.0 (dotted).

LILAC simulation. Significant deviation is observed during the main pulse for the standard flux-limited heat-conduction model with inverse bremsstrahlung (dashed-dot). In this case, the target is overdriven with a total absorption fraction of 86% compared to the measured value of $(75 \pm 1)\%$. This difference can be explained assuming the cross-beam transfer of energy induced by SBS. To show the sensitivity of the observables to cross-beam effects, two different overall multipliers (0.5 and 1.0) were used for the cross-beam model in simulation [multiplier of 0.5 (dashed); multiplier of 1.0 (dotted)]. The time-integrated absorption fraction decreases to 78% and 73%, respectively, with these multipliers. In addition, better agreement was obtained with the time-resolved scattered light data [Fig. 8(a)] when the cross-beam transfer model was used. The experimental neutron-production histories were measured by the neutron temporal diagnostic (NTD).[24] The observed neutron rate is 140 ± 50 ps delayed relative to the simulated rate for the standard model (dashed-dot), indicating loss of laser drive. Similar delays in neutron production are also evident in measurements of x-ray emission using DANTE.[25] Better agreement with the neutron-rate
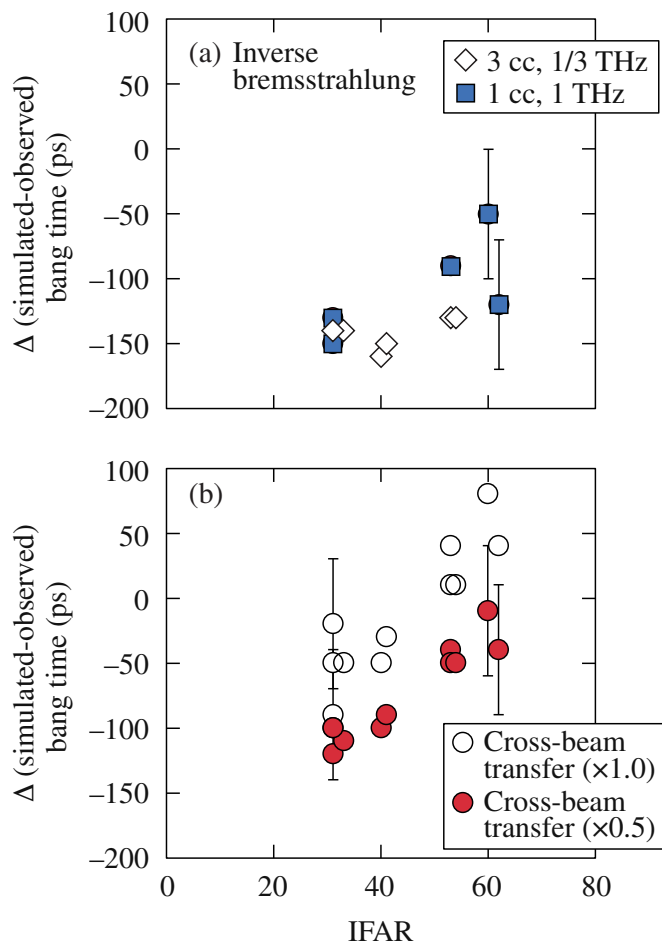
FIG. 9. (Color online) Difference in bang time (simulated-observed) for the various implosions for differing models vs simulated IFAR. (a) Flux-limited heat-conduction model [3 cc, 1/3 THz system (open diamonds); 1 cc, 1 THz system (solid squares)]; (b) model including cross-beam energy transfer with a multiplier of 1.0 (open circles); model including cross-beam energy transfer with a multiplier of 0.5 (solid circles) for both smoothing systems. The error bars represent a typical error in the measured time of neutron production.

measurement was also obtained with the cross-beam model, the best agreement with a multiplier of 1.0 (dotted). The simulated implosion velocity decreases by ∼8% for this reduction in absorbed energy.

The summary over all shots of the difference in the neutron-production times [defined as the difference in 1D-simulated and measured time when the neutron rate exceeds the noise level (5×10^{18} neutrons/s)] is shown in Fig. 9(a) for the standard model. No significant difference is observed between the 3 cc, 1/3 THz (open) and 1 cc, 1 THz (solid) smoothing systems. The typical error in the timing measurement for the neutron-production times is shown (±50 ps). The cross-beam transfer model results are summarized in Fig. 9(b) for both smoothing systems. Since there is no significant difference between the two in bang times, the summary in Fig. 9(b) does not distinguish between them. The agreement improves when cross-beam effects are included; better agreement is obtained with the multiplier of 1.0 (open circles) for the cross-beam transfer model compared to the model with the multiplier of 0.5 (solid circles). The comparison of neutron bang time between 1D simulation and experi-

ment is complicated by the earlier neutron production for significantly distorted shells. Figure 9(b) suggests a trend with IFAR; as IFAR increases, the measured bang time advances relative to the 1D simulation. For IFAR ∼ 60, the experimentally measured rates are advanced relative to simulation by 50–80 ps, consistent with the trend in 2D simulations.

Since the multiplier of 1.0 gives the best agreement with both scattered light and bang time, it is used in all the subsequent simulations. For comparison, the flux-limited model results with no beam transfer are also shown. Simulated and observed yields are shown in Figs. 10(a) and 10(b) for the 3 cc and 1 cc smoothing systems, respectively. For both smoothing techniques, the measured yields (open and right axis) decrease as IFAR increases, whereas yields from spherically symmetric (1D) simulations of the implosion experiments show the opposite trend [cross-beam transfer model (red); standard model (black)]. The degradation of target performance with IFAR is further quantified in Fig. 10(c) for both smoothing systems. The observed yield as a fraction of this simulated yield decreases with increasing IFAR. The degradation is independent of smoothing systems (squares—3 cc; diamonds—1 cc). As the 2D simulations in Fig. 7 indicate, this decrease arises from the growth of shorter wavelengths for the higher IFAR. The ratio of the measured to the simulated yield improves ∼20%–30% with the cross-beam transfer model (open symbols). This is due to the lower implosion velocity and, consequently, lower predicted ion temperatures and neutron yields. The trend in the yield ratio is consistent with the trend from 2D simulations [Fig. 7(a)]. However, simulated 2D absolute values of the yield ratio are higher than the observed values. This may be caused by other sources of nonuniformity not included in the simulations, such as the stalk used to suspend the target, defects and dust on the target, and three-dimensional effects.

The trend in target performance with IFAR is reflected in the observed and simulated areal densities. Figures 11(a) and 11(b) show the observed (open) and the simulated values [cross-beam transfer (red); standard model (black)] of neutron-averaged areal density for the 3 cc and 1 cc system, respectively. Either five or six wedged range filters at different angles around the target were used to measure the emerging secondary proton spectrum from the target.[26] The areal density is proportional to the energy loss of these protons in the target and is inferred by knowing the birth spectrum and therefore the energy loss. The observed values are the average of the areal-density values inferred at different angles around the target, and the error bars represent the standard deviation of this variation in areal density. Simulated areal densities increase with increasing IFAR, whereas measured values decrease with increasing IFAR. Figure 11(c) shows the fraction of areal density to the simulated values, which decrease with increasing IFAR for both smoothing techniques. The experimentally inferred ratio (∼60% of 1D) is very similar to that modeled by the 2D simulation (∼70% of 1D). Since areal density is determined primarily by the adiabat (which is set by the shocks earlier in the pulse) and depends weakly on the laser energy [Eq. (5)], the late time reduction in laser drive associated with cross-beam transfer
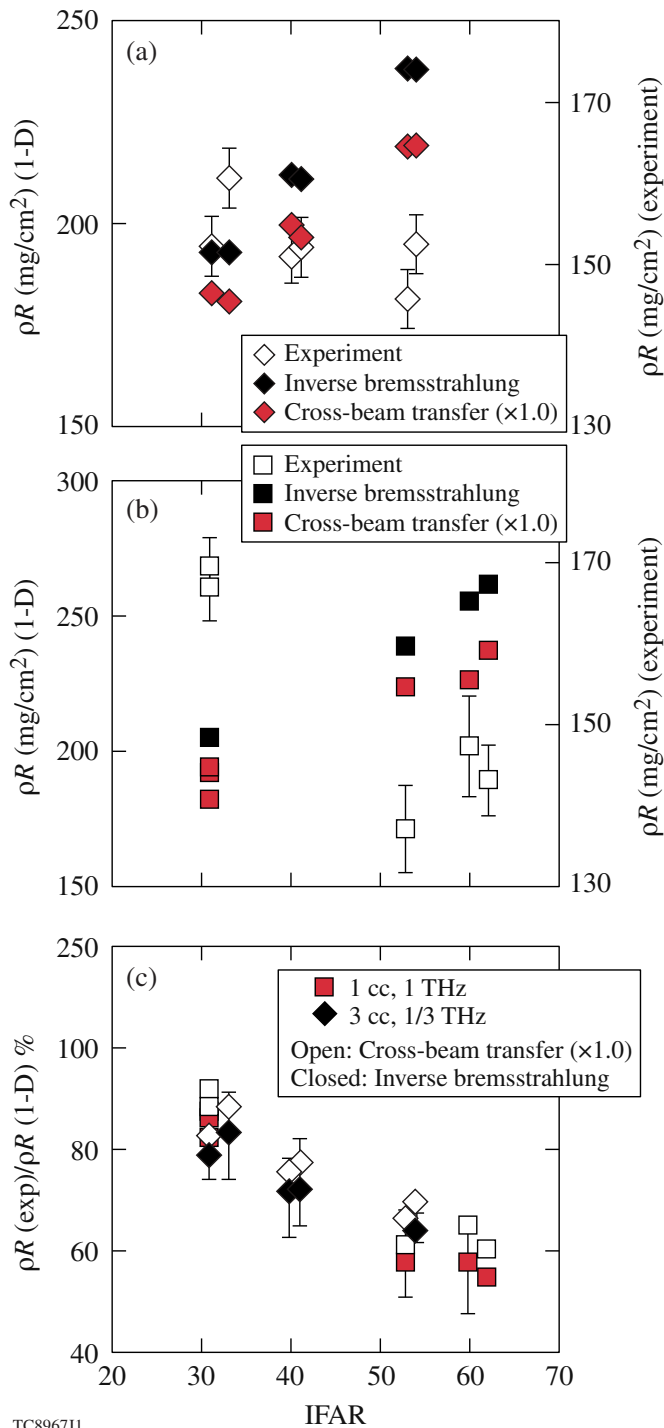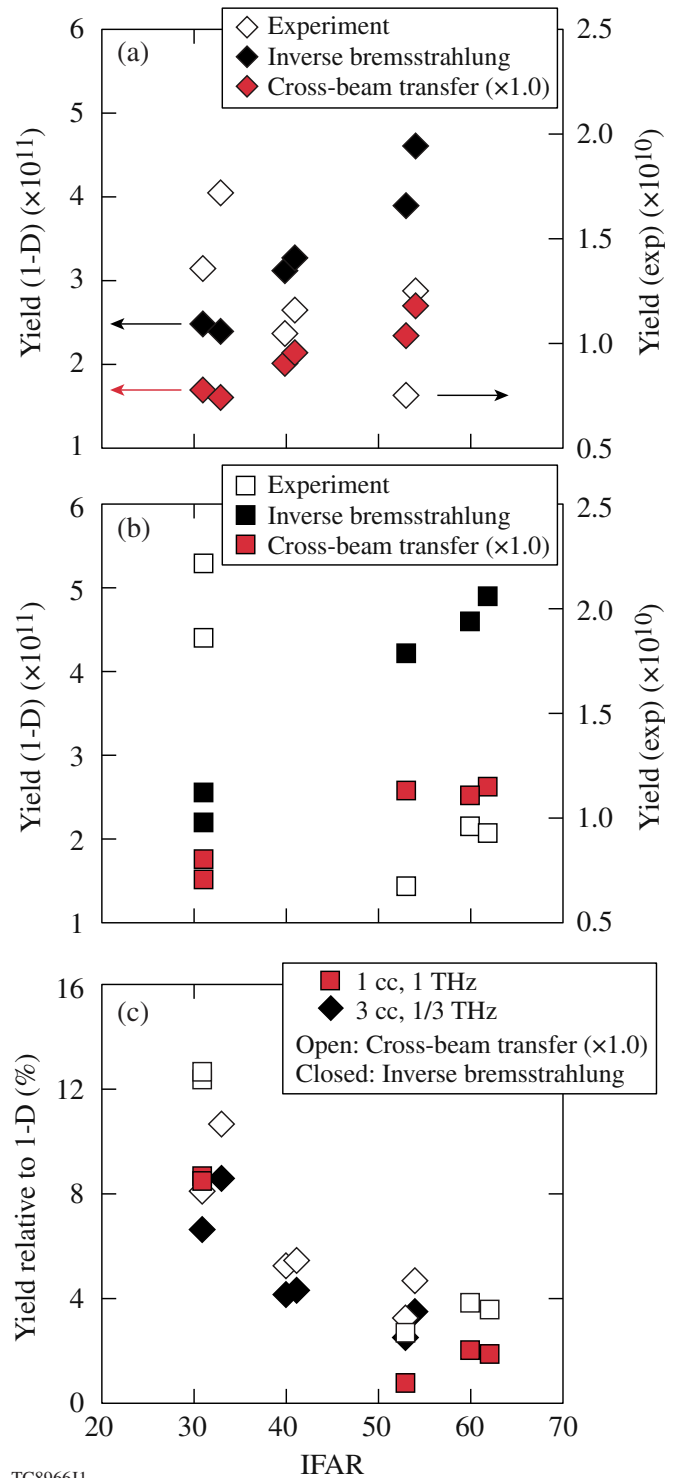
FIG. 10. (Color online) (a) Yield from spherically symmetric simulations [left axis (solid)] and measured yield [right axis (open)] vs the calculated IFAR for the 3 cc, 1/3 THz laser-smoothing system. (b) Same as (a) but for the 1 cc, 1 THz smoothing system. (c) Ratio of observed yield to the simulated yield vs IFAR [3 cc, 1/3 THz (diamonds); 1 cc, 1 THz (squares)].

FIG. 11. (Color online) (a) Neutron-averaged areal density from spherically symmetric simulations [left axis (solid circle)] and measured areal densities [right axis (open circle)] vs the calculated IFAR for the 3 cc, 1/3 THz laser-smoothing system. (b) Same as (a) but for the 1 cc, 1 THz smoothing system. (c) Ratio of observed areal density to the simulated areal density vs IFAR [3 cc, 1/3 THz (diamonds); 1 cc, 1 THz (squares)].

has a marginal effect on areal density. There is no significant difference in the extent of areal-density variations around the target for the two smoothing systems; the error bars for the red squares (1 cc, 1 THz) are comparable to those for the black diamonds (3 cc, 1/3 THz).

The areal density can be diagnosed only during the time of neutron production since fusion products are used to infer areal density. This introduces an additional complication

when compared to simulation, as shown in Figs. 12(a) and 12(b) for IFAR ∼ 31 and IFAR ∼ 60, respectively. The measured time history of neutron production [left axis (solid)] is typically truncated relative to 1D neutron-production histories [left axis (dotted)]. Truncation of the neutron rate occurs
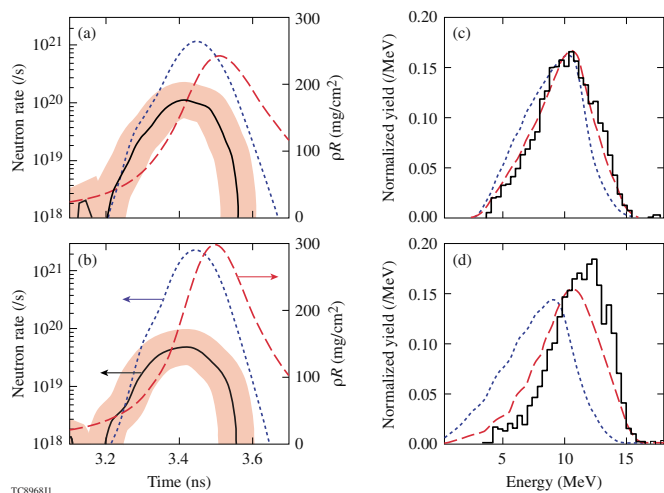
FIG. 12. (Color online) (a) Left axis: measured neutron rate (solid) and simulated neutron rate (dashed-dotted) for the IFAR~31 implosion. Right axis: simulated areal-density history (b) same as (a) but for the IFAR~60 implosion. (c) Measured secondary proton spectrum (solid) and simulated secondary proton spectrum (dotted) for the IFAR~31 implosion. Also shown is the simulated spectrum using the measured neutron rate (dashed). (d) Same as (c) but for the IFAR~60 implosion.
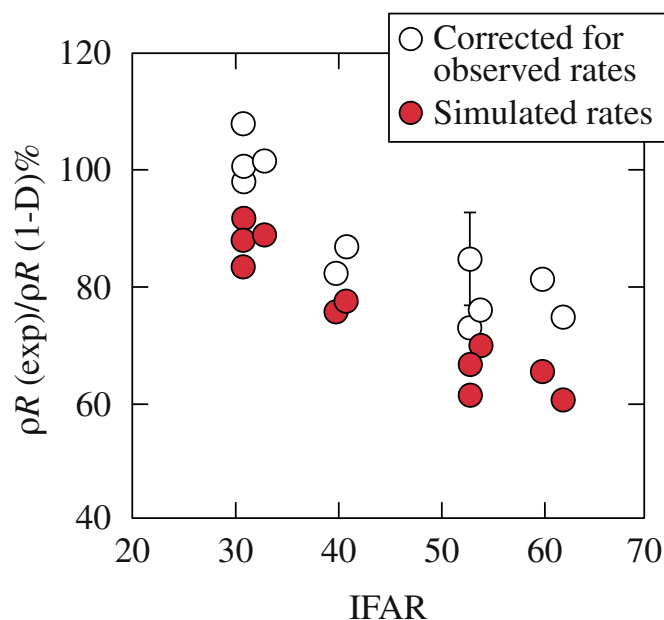

FIG. 13. (Color online) Ratio of observed areal density to the simulated yield vs IFAR without the correction for the observed neutrons (solid) and with correction of observed neutrons (open). The error bars indicate the typical range in this ratio for a ±25 ps change in neutron-rate timing.

because of instability growth at the plastic-gas interface and the flow of D_2 fuel into the colder bubbles.[22] The simulated areal-density history [right axis (dashed)] is also shown in Figs. 12(a) and 12(b). To appropriately account for the sampling of the areal density, the experimentally observed neutron-burn-rate is used to calculate the secondary proton spectrum. The Monte Carlo particle tracking code *IRIS* (Ref. 27) is used as a postprocessor to LILAC to calculate the secondary proton spectra using the self-consistent rates calculated by LILAC and the measured neutron rates. Figures 12(c) and 12(d) show the LILAC simulation (dotted) and measured neutron-burn-rate, postprocessed secondary proton spectrum (dashed). Since the absolute timing is typically known to only ±50 ps, the timing between the measurement and the simulation is instead chosen by aligning the NTD signal with the onset of the compression yield in the simulation. A shift of about 50 ps in the neutron rate (within the experimental error bars) results in about a 0.5 MeV shift in the spectrum under these density and temperature conditions corresponding to a change of 10%–15% in the areal density. With this correction, significantly better agreement with measurement is obtained for the IFAR~31 implosion compared to the IFAR~60 implosion. Burn truncation reduces the value of the predicted areal densities by 10%–20%. Figure 13 shows the ratio of the measured to the simulated areal densities corrected (open circles) and not corrected (solid circles) for the measured neutron-production histories. The error bars represent the different values inferred for a ±25 ps variation in timing. IFAR~31 implosions reproduce simulated values, whereas the IFAR~60 implosions reproduce only ~80% of the simulated value with the correction.

Neutron-averaged ion temperatures, defined by the width of the neutron time-of-flight spectrum,[28] show unclear trends with IFAR (Fig. 14). The error in the measured ion temperatures is ~0.5 keV, too large for absolute comparisons with

simulation to yield any insight into the implosion; however, the error is estimated to be smaller, ~5%, between consecutive shots. For both smoothing systems, simulated ion temperatures increase with IFAR, whereas the trend in measured ion temperatures is unclear even with these errors. Two-dimensional simulations indicate that ion temperatures should decrease with increasing IFAR.

The sensitivity of target performance to laser speckle was studied by turning off SSD beam smoothing on the OMEGA system. This increased the nonuniformity seeds for RT growth, resulting in larger distortions of the accelerating shell. When beam smoothing was turned off, the observed yields relative to 1D fell to 0.75% compared to 2.0% for the 1 cc, 1 THz smoothing for the implosion with IFAR~60. The observed areal density decreased from 140 to 102 mg/cm² for the IFAR~60 implosion, which is 40% of the 1D value compared to 67% of the 1D value when full beam smoothing was used. This indicates that the IFAR ~60 implosions are indeed sensitive to short wavelengths through laser imprint.

That IFAR≤40 is required to achieve adequate, near-1D compression must be regarded as a conservative upper limit on the IFAR. Evidence from experiments on RT growth at higher intensities of 1×10^{15} W/cm² indicates reduced ablative growth rates than calculated using standard simulations, which exclude preheat.[21] This has been attributed to preheating of the ablation surface caused by nonlocal transport of energetic electrons from the tail of their distribution function in the corona. The effect at a lower intensity of 8×10^{14} W/cm²—used for OMEGA cryogenic implosions and the ignition design for the National Ignition Facility—is still unclear. It is possible that in the presence of such preheat, shorter wavelengths may not compromise the implosion as significantly as shown in this paper at an intensity of
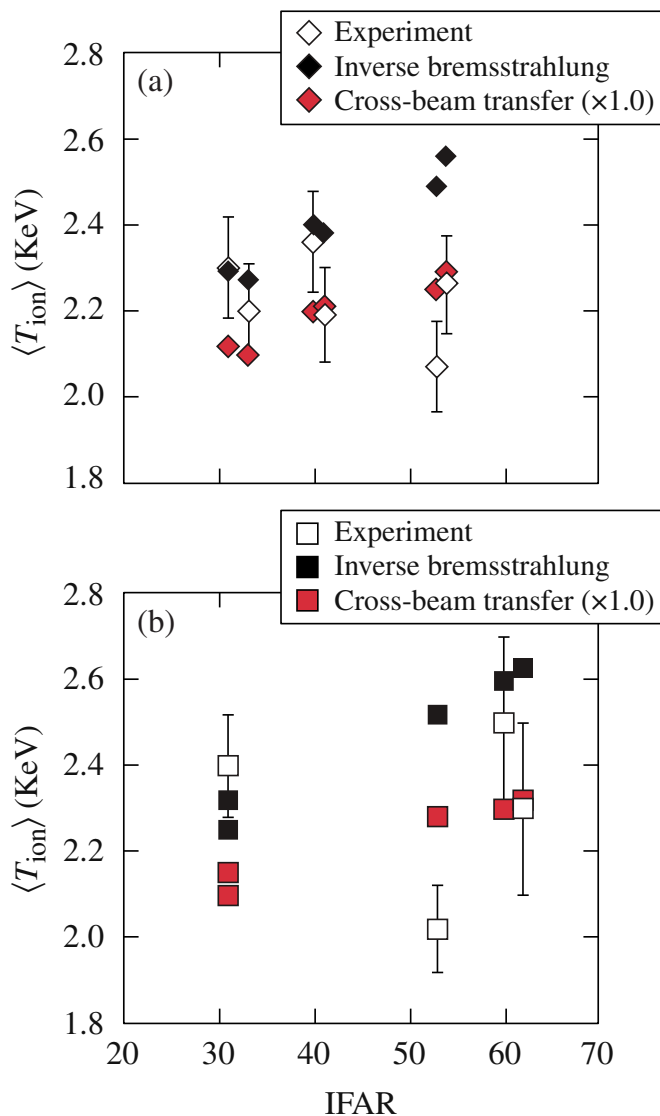
FIG. 14. (Color online) (a) Observed ion temperature (open) and simulated ion temperature (closed) vs IFAR for the 3 cc, 1/3 THz system. (b) Same as in (a) but for the 1 cc, 1 THz smoothing system. The error bars indicate the estimated precision in measured ion temperatures (5%) for consecutive shots.

$\sim 4.5 \times 10^{14}$ W/cm^2, allowing larger values of IFAR at 8×10^{14} W/cm^2. Future experiments will investigate this effect by studying implosions at higher intensities where such preheat is possible.

IV. CONCLUSIONS

Triple-picket pulses were used to irradiate warm, 27-μm-thick plastic (CH) shells filled with 9 atm of D$_2$ gas. Picket energies and the timings between the pickets were varied to obtain differing IFARs. The delay in the observed neutron bang time relative to simulations is consistent with a model for cross-beam transfer of laser energy. This model reproduces observations of neutron bang times and temporally resolved scattered light for the range of implosions presented in this work. Two-dimensional simulations indicate that the shell during acceleration for an IFAR$\sim$60 implosion should be broken and the areal density significantly reduced,

consistent with observations. When the IFAR was reduced in the experiment, areal density increased significantly to 170 mg/cm^2, nearly 85% of the spherically symmetric (or 1D) simulation. DRACO simulations indicate that the shell for an IFAR$\sim$31 implosion should be significantly more intact and should achieve near-1D compression. The observed neutron yields increased by a little over a factor of 2 when IFAR was decreased from $\sim$60 to $\sim$31, contrary to spherically symmetric simulations. This indicates poor in-flight shell stability for the implosion with IFAR$\sim$60 and improved stability for the IFAR$\sim$31 implosion. Imprint efficiencies for the design considered in this work were very similar to those for triple-picket cryogenic designs.[20] Since the ablator material in this design is very similar to the ablator in the cryogenic design, similar growth rates are to be expected for similar IFARs in the two designs. This suggests that to compress adequately, it is important to keep the IFAR below 40 in a directly driven cryogenic implosion. As mentioned earlier, this technique will be used to study higher-intensity implosions in the presence of potential preheat of the ablation surface. That series of implosions will also be used to identify the effect of preheat attributable to energetic electrons at higher intensities caused by TPD and for high-convergence polar-drive[29] studies on OMEGA.

ACKNOWLEDGMENTS

[1] J. D. Lindl, *Inertial Confinement Fusion: The Quest for Ignition and Energy Gain Using Indirect Drive* (Springer-Verlag, New York, 1998).
[2] M. C. Herrmann, M. Tabak, and J. D. Lindl, Nucl. Fusion **41**, 99 (2001).
[3] Lord Rayleigh, Proc. London Math. Soc. **XIV**, 170 (1883); G. Taylor, Proc. R. Soc. London, Ser. A **201**, 192 (1950).
[4] R. Kishony and D. Shvarts, Phys. Plasmas **8**, 4925 (2001).
[5] R. Betti, V. N. Goncharov, R. L. McCrory, and C. P. Verdon, Phys. Plasmas **5**, 1446 (1998); H. Takabe, K. Mima, L. Montierth, and R. L. Morse, Phys. Fluids **28**, 3676 (1985).
[6] C. D. Zhou and R. Betti, Phys. Plasmas **14**, 072703 (2007).
[7] V. N. Goncharov, T. C. Sangster, T. R. Boehly, S. X. Hu, I. V. Igumenshchev, F. J. Marshall, R. L. McCrory, D. D. Meyerhofer, P. B. Radha, W. Seka, S. Skupsky, C. Stoeckl, D. T. Casey, J. A. Frenje, and R. D. Petrasso, Phys. Rev. Lett. **104**, 165001 (2010).
[8] R. Betti, P. Y. Chang, B. K. Spears, K. S. Anderson, J. Edwards, M. Fatenejad, J. D. Lindl, R. L. McCrory, R. Nora, and D. Shvarts, Phys. Plasmas **17**, 058102 (2010).
[9] LLE Review Quarterly Report, LLE Document No. DOE/NA/28302-953LLE, Laboratory for Laser Energetics, University of Rochester, 2010.
[10] R. Betti and C. Zhou, Phys. Plasmas **12**, 110702 (2005).
[11] V. N. Goncharov, J. P. Knauer, P. W. McKenty, P. B. Radha, T. C. Sangster, S. Skupsky, R. Betti, R. L. McCrory, and D. D. Meyerhofer, Phys. Plasmas **10**, 1906 (2003); R. Betti, K. Anderson, J. Knauer, T. J. B. Collins, R. L. McCrory, P. W. McKenty, and S. Skupsky, *ibid.* **12**, 042703 (2005).
[12] T. R. Boehly, V. N. Goncharov, W. Seka, D. E. Fratanduono, M. A. Barrios, S. X. Hu, J. A. Marozas, T. C. Sangster, D. D. Meyerhofer, D. G. Hicks, and P. M. Celliers, Bull. Am. Phys. Soc. **54**, 305 (2009).
[13] A. Simon, R. W. Short, E. A. Williams, and T. Dewandre, Phys. Fluids **26**, 3107 (1983).
[14] P. B. Radha, V. N. Goncharov, T. J. B. Collins, J. A. Delettrez, Y. Elbaz, V.

Yu. Glebov, R. L. Keck, D. E. Keller, J. P. Knauer, J. A. Marozas, F. J. Marshall, P. W. McKenty, D. D. Meyerhofer, S. P. Regan, T. C. Sangster, D. Shvarts, S. Skupsky, Y. Srebro, R. P. J. Town, and C. Stoeckl, Phys. Plasmas **12**, 032702 (2005).

[15] J. Delettrez, R. Epstein, M. C. Richardson, P. A. Jaanimagi, and B. L. Henke, Phys. Rev. A **36**, 3926 (1987).

[16] T. R. Boehly, D. L. Brown, R. S. Craxton, R. L. Keck, J. P. Knauer, J. H. Kelly, T. J. Kessler, S. A. Kumpan, S. J. Loucks, S. A. Letzring, F. J. Marshall, R. L. McCrory, S. F. B. Morse, W. Seka, J. M. Soures, and C. P. Verdon, Opt. Commun. **133**, 495 (1997).

[17] S. Skupsky, R. W. Short, T. Kessler, R. S. Craxton, S. Letzring, and J. M. Soures, J. Appl. Phys. **66**, 3456 (1989).

[18] See National Technical Information Service Document No. DE96011927, Laboratory for Laser Energetics LLE Review Quarterly Report, 1995. Copies may be obtained from the National Technical Information Service, Springfield, VA 22161.

[19] T. R. Boehly, V. A. Smalyuk, D. D. Meyerhofer, J. P. Knauer, D. K. Bradley, R. S. Craxton, M. J. Guardalben, S. Skupsky, and T. J. Kessler, J. Appl. Phys. **85**, 3444 (1999).

[20] S. X. Hu, V. N. Goncharov, P. B. Radha, J. A. Marozas, S. Skupsky, T. R. Boehly, T. C. Sangster, D. D. Meyerhofer, and R. L. McCrory, "Two-dimensional simulations of the neutron yield in cryogenic-DT implosions on OMEGA," Phys. Plasmas **17**, 102706 (2010).

[21] V. A. Smalyuk, S. X. Hu, V. N. Goncharov, D. D. Meyerhofer, T. C. Sangster, C. Stoeckl, and B. Yaakobi, Phys. Plasmas **15**, 082703 (2008).

[22] P. B. Radha, T. J. B. Collins, J. A. Delettrez, Y. Elbaz, R. Epstein, V. Yu. Glebov, V. N. Goncharov, R. L. Keck, J. P. Knauer, J. A. Marozas, F. J. Marshall, R. L. McCrory, P. W. McKenty, D. D. Meyerhofer, S. P. Regan, T. C. Sangster, W. Seka, D. Shvarts, S. Skupsky, Y. Srebro, and C. Stoeckl, Phys. Plasmas **12**, 056307 (2005).

[23] W. Seka, D. H. Edgell, J. P. Knauer, J. F. Myatt, A. V. Maximov, R. W. Short, T. C. Sangster, C. Stoeckl, R. E. Bahr, R. S. Craxton, J. A. Delettrez, V. N. Goncharov, I. V. Igumenshchev, and D. Shvarts, Phys. Plasmas **15**, 056312 (2008).

[24] R. A. Lerche, D. W. Phillion, and G. L. Tietbohl, Rev. Sci. Instrum. **66**, 933 (1995).

[25] H. N. Kornblum, R. L. Kauffman, and J. A. Smith, Rev. Sci. Instrum. **57**, 2179 (1986); K. M. Campbell, F. A. Weber, E. L. Dewald, S. H. Glenzer, O. L. Landen, R. E. Turner, and P. A. Waide, *ibid.* **75**, 3768 (2004); C. Sorce, J. Schein, F. Weber, K. Widmann, K. Campbell, E. Dewald, R. Turner, O. Landen, K. Jacoby, P. Torres, and D. Pellinen, *ibid.* **77**, 10E518 (2006).

[26] F. H. Séguin, C. K. Li, J. A. Frenje, D. G. Hicks, K. M. Green, S. Kurebayashi, R. D. Petrasso, J. M. Soures, D. D. Meyerhofer, V. Yu. Glebov, P. B. Radha, C. Stoeckl, S. Roberts, C. Sorce, T. C. Sangster, M. D. Cable, K. Fletcher, and S. Padalino, Phys. Plasmas **9**, 2725 (2002).

[27] P. B. Radha, J. A. Delettrez, R. Epstein, S. Skupsky, J. M. Soures, S. Cremer, and R. D. Petrasso, Bull. Am. Phys. Soc. **44**, 194 (1999).

[28] D. D. Meyerhofer, J. A. Delettrez, R. Epstein, V. Yu. Glebov, V. N. Goncharov, R. L. Keck, R. L. McCrory, P. W. McKenty, F. J. Marshall, P. B. Radha, S. P. Regan, S. Roberts, W. Seka, S. Skupsky, V. A. Smalyuk, C. Sorce, C. Stoeckl, J. M. Soures, R. P. J. Town, B. Yaakobi, J. D. Zuegel, J. Frenje, C. K. Li, R. D. Petrasso, D. G. Hicks, F. H. Séguin, K. Fletcher, S. Padalino, C. Freeman, N. Izumi, R. Lerche, T. W. Phillips, and T. C. Sangster, Phys. Plasmas **8**, 2251 (2001).

[29] S. Skupsky, J. A. Marozas, R. S. Craxton, R. Betti, T. J. B. Collins, J. A. Delettrez, V. N. Goncharov, P. W. McKenty, P. B. Radha, T. R. Boehly, J. P. Knauer, F. J. Marshall, D. R. Harding, J. D. Kilkenny, D. D. Meyerhofer, T. C. Sangster, and R. L. McCrory, Phys. Plasmas **11**, 2763 (2004).